Balanced-fed planar antenna for millimeter-wave transceivers

Balanced-Fed Planar Antenna for Millimeter-Wave Transceivers

Johannes A. G. Akkermans, Matti H. A. J. Herben, *Senior Member, IEEE*, and Martijn C. van Beurden

***Abstract*—A balanced antenna design is presented that is tailored to broadband communication in the 60-GHz frequency band. The antenna can be realized in printed circuit-board technology, has a high radiation efficiency and can be used in array configurations. It is modeled with a method-of-moments implementation. The radiation efficiency is analyzed in detail, and design guidelines are given. Moreover, an optimization method is outlined that optimizes both antenna bandwidth and radiation efficiency. The antenna element and a circular antenna array have been realized. Measurements of these antennas are in good agreement with simulated results.**

***Index Terms*—Antenna arrays, antenna efficiency, antenna measurements, antenna optimization, millimeter-wave antenna, millimeter-wave antenna arrays, millimeter wave antennas, optimization methods.**

I. Introduction

THERE is an increasing demand for low-cost wireless communication systems that support data rates of gigabits per second (Gb/s), for example, in applications such as wireless gigabit Ethernet and wireless uncompressed high-definition video. The success of these types of applications very much depends on the cost of a single transceiver. Therefore, it is important to realize low-cost transceiver designs. To be able to transmit gigabits per second, a lot of spectral space is needed, and this explains the increasing interest to use the license-free frequency band around 60 GHz. The 60-GHz frequency band has an available bandwidth of about 7-GHz worldwide. For example, the United States allocated the frequency band from 57 to 64 GHz [1], and in Europe a 9-GHz bandwidth from 57 to 66 GHz is recommended. Wireless systems that use this frequency band have the potential to achieve data rates of multiple gigabits per second.

Advances in silicon manufacturing technology allow the realization of RF front ends that operate at 60 GHz in CMOS technology [2], which results in a low-cost solution for the front end. To fulfill the link budget requirements needed for Gb/s transmission in the 60-GHz band, front ends with several power amplifiers are needed to generate the required transmit power at 60 GHz. Additionally, antennas need to be employed that have sufficient gain and that are capable of beam-forming [3], which requires the realization of antenna arrays. Integration of the front end with the antenna should be given careful consideration at these relatively high frequencies to minimize interconnection losses [4]. A balanced interconnection between the front end and the antenna allows for a completely balanced design of the front end, which can significantly improve the performance of the transceiver. Therefore, a balanced antenna design is desirable. Moreover, an antenna design is needed that covers the entire available bandwidth and that has a high radiation efficiency to obtain a power-efficient transceiver. To allow for a simple integration with the front end, and a low-cost antenna design, a standard planar manufacturing technology is preferable.

The main challenge of antenna design in a planar technology is the tradeoff between radiation efficiency and bandwidth. To obtain a large bandwidth, a relatively thick dielectric layer is needed [5]. However, a thicker dielectric layer introduces higher loss due to surface-wave excitation in the dielectric. A lot of work has been done to improve the radiation efficiency of planar antennas while maintaining a large bandwidth [6], [7]. Particularly, the use of electromagnetic bandgap (EBG) materials that suppress the surface-wave excitation has received a lot of attention [8]–[10]. However, EBG materials are either difficult to manufacture, or too large to be used in planar array configurations. Another approach to improve the radiation efficiency is presented in [11], where a superstrate antenna is used. This solution shows good performance but is more complicated to realize since the superstrate antenna is a separate component that has to be placed partly on top of the integrated circuit.

As an alternative, a balanced antenna design is proposed here. In this design, the antenna element itself cancels part of the surface-wave excitation. Because of the reduced surface-wave excitation, a simulated radiation efficiency of over 80% is obtained throughout the band of operation. On top of that, an antenna bandwidth of more than 10% is realized by using two resonant elements. The resulting design is completely planar, and the use of vias is avoided. The width and length of the antenna is less than half a free-space wavelength, such that the antenna can be readily used for the realization of a planar beam-forming array [12]. The modeling of the antenna and the analysis of the radiation efficiency is presented in [13]. Here, this model is validated, and the antenna design is analyzed in more detail. To maximize the performance of the antenna and to simplify the design procedure, design guidelines are given and an optimization procedure is outlined and applied as well.

Manuscript received May 26, 2008; revised July 31, 2008. First published August 04, 2009; current version published October 07, 2009. This work is part of the SiGi-Spot project (IGC0503) that is funded by the Dutch ministry of Economic affairs within the IOP-GenCom program.

J. A. G. Akkermans was with Eindhoven University of Technology, Eindhoven 5658, The Netherlands. He is now with ASML Research, Veldhoven, The Netherlands (e-mail: iwan@akkermans-wireless.nl).

M. H. A. J. Herben and M. C. van Beurden are with the Electromagnetics and Wireless Group, Eindhoven University of Technology, Eindhoven 5658, The Netherlands.

Color versions of one or more of the figures in this paper are available online at http://ieeexplore.ieee.org.

Digital Object Identifier 10.1109/TAP.2009.2029278

The geometry of the antenna is discussed in Section II. To model the antenna, a method-of-moments implementation is outlined in Section III. The radiation efficiency and the front-to-back ratio of the antenna are considered in Sections IV and V, respectively. An optimization method for antenna bandwidth and radiation efficiency is presented in Section VI. Measurement results for the single-element antenna are presented in Section VII. Measured radiation patterns of a six-element antenna array are presented in Section VIII and, finally, conclusions are drawn in Section IX.

II. Antenna Design

The antenna design is based on a balanced-fed aperture-coupled patch antenna [14], which is an aperture-coupled patch antenna with two apertures (slots) that couple to a balanced feed. Aperture-coupled patch antennas have the advantage that they can be easily integrated with active electronics since substrate properties of the feed line can be chosen independently from the substrate properties of the radiating patch [15].

A disadvantage of aperture-coupled patch antennas is the back radiation that is caused by the ground plane in which the slots lie. To reduce the back radiation, a microstrip antenna element is placed behind the slots. This element acts as a reflector [16]. It can be placed at a distance from the slots that is much smaller than $\lambda_d/4$, with λ_d the wavelength in the dielectric. Therefore, the thickness of the dielectric below the slots remains small in terms of wavelengths and the excitation of surface-waves is limited. To reduce the back radiation effectively, the size of the reflector element is adjusted [16]. The performance of the reflector element is analyzed in Section V.

The two slots play an important role in the antenna design. First, they are used to reduce the surface-wave excitation in the dielectric. The slots are positioned such that the surface waves that are generated by the slots and the patch interfere destructively, and, therefore, the radiation efficiency of the antenna is improved. An analysis of the radiation efficiency of two distant slots is presented in [17]. In Section IV, the analysis is extended to the case in which both slots and a patch are present. Second, the slots are used to improve the antenna bandwidth. The slots can be resonant in the operation band of the antenna because the reflector element compensates for the back radiation. As a result, the bandwidth is increased significantly since the antenna now has two resonant elements with slightly different resonance frequencies, i.e., the patch and both slots. An increase is observed from about 3% for the conventional single-element patch to more than 10% for this design.

The proposed antenna design combines the use of two separate slots with the use of the reflector element. The resulting design has a high radiation efficiency and a low back radiation. The geometry of the antenna element is shown in Figs. 1 and 2. The antenna can be realized from two PCB boards with metallization on both sides that are stacked with a glue layer (prepreg) in between. The important parameters in the design of the antenna are the length of the slots, the spacing between the slots, the length of the patch, and the length of the dipole underneath the slots. The length of the slots and the length of the patch determine the operation bandwidth of the antenna. The spacing between the slots determines the radiation efficiency of the antenna and the coupling between the slots and the patch, as will be clarified in Section IV. The length of the dipole underneath the slots is important for the impedance matching of the antenna with respect to the front-end.

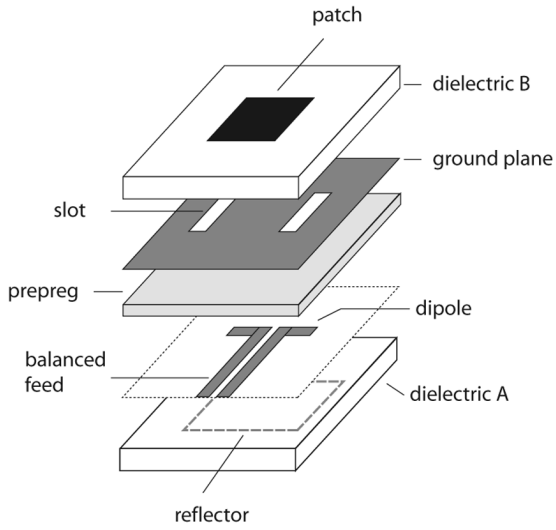

Fig. 1. Geometry of the balanced-fed aperture-coupled patch antenna with reflector element.

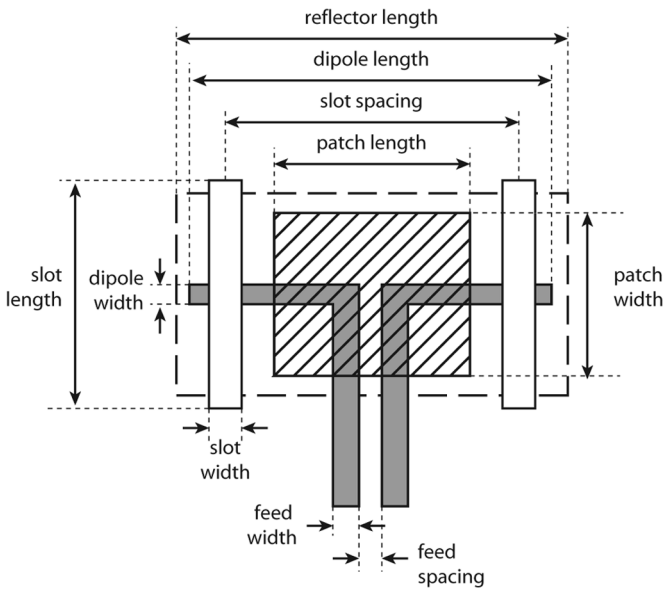

Fig. 2. Top view of the antenna with accompanying design dimensions.

III. Modeling Approach

The antenna is analyzed with a method-of-moments (MoM) approach. Both subdomain and entire-domain basis functions are used to obtain a model with a limited number of unknowns. This reduces the computational effort that is needed to analyze the performance of the antenna, and it allows us to employ an efficient optimization algorithm (see Section VI). The formulation relies on the Green's functions for layered media and does not include the influence of the finite lateral dimensions of the dielectric layers. For normal board sizes, the finite-size dielectric substrate does not affect the impedance matching of the antenna. At the edges of the finite size dielectric layer, the surface waves scatter and distort the radiation pattern. As a result of this, a ripple will be superimposed on the radiation pattern

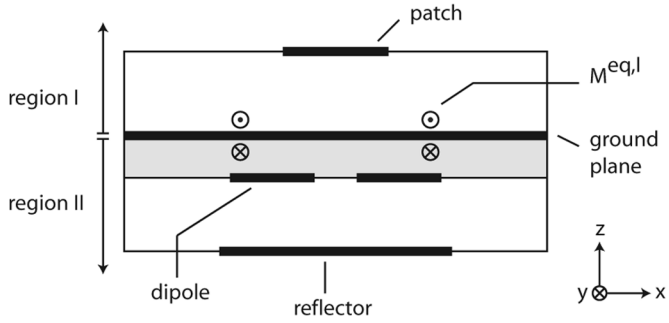

Fig. 3. Equivalent problem of the balanced-fed aperture-coupled patch.

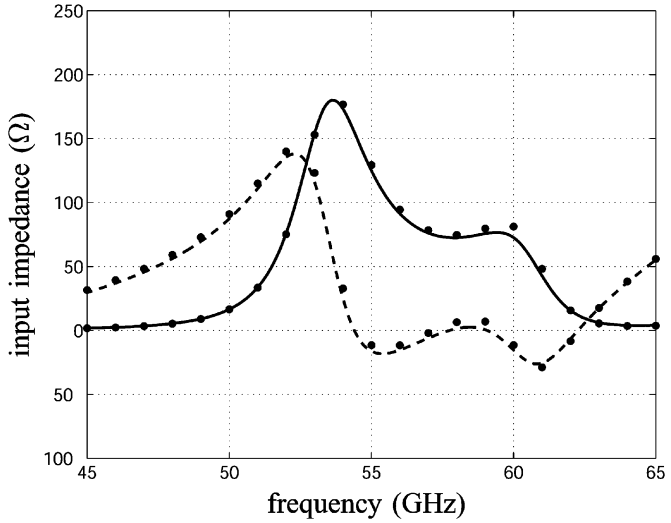

Fig. 4. Antenna input impedance. Ansoft Designer: $\Re\{Z_{\text{in}}\}$ (solid), $\Im\{Z_{\text{in}}\}$ (dashed), and MoM model: (dots). Dimensions in Table I.

[18]. This effect will be analyzed separately and is discussed in Section VII.

The metal layers have been modeled as perfect electric conductors. The feed structure below the ground plane and the antenna structure above the ground plane can be analyzed separately if Schelkunoff's equivalence principle is employed [19]. Equivalent magnetic currents $\mathbf{M}^{\text{eq},i}$ are introduced to represent the aperture fields in region i[20]. The equivalent problem is shown in Fig. 3. For the simulations, Galerkin's procedure has been employed. The electric current density on the patch and on the reflector element has been modeled with entire-domain expansion and testing functions, whereas the current on the dipole is modeled with rooftop basis functions [13]. Since the coupled microstrip line that is connected to the dipole hardly contributes to the radiation of the structure, it is not accounted for in the analysis. The dipole is excited with a delta-gap source in the middle.

The currents on the metal layers are obtained from the electric field integral equation, whereas the equivalent magnetic currents are obtained from the magnetic field integral equation. Closed-form expressions for Green's functions in layered media have been derived in the spectral domain [21], [22]. These functions are employed to calculate the electric and magnetic fields in the two separate regions.

Using typical notation for MoM analysis, the discretized electromagnetic (EM) problem is denoted as

$$\mathbf{ZI} = \mathbf{V} \tag{1}$$

and this can be expanded in terms of contributions from electric and magnetic currents as

$$\begin{bmatrix} \mathbf{Z}^{JJ} & \mathbf{Z}^{JM} \\ \mathbf{Z}^{MJ} & \mathbf{Z}^{MM} \end{bmatrix} \begin{bmatrix} \mathbf{I}^{J} \\ \mathbf{I}^{M} \end{bmatrix} = \begin{bmatrix} \mathbf{V}^{J} \\ \mathbf{0} \end{bmatrix} \tag{2}$$

where $\mathbf{Z}^{PQ}$ represents an interaction matrix, which measures the interaction between the expansion function $\mathbf{Q}$ and test function $\mathbf{P}$. The vectors $\mathbf{I}^{J}$ and $\mathbf{I}^{M}$ represent complex coefficients of the electric and magnetic current density, respectively. The excitation vector $\mathbf{V}^{J}$ represents the source in the EM problem.

TABLE I
DIMENSIONS AND DIELECTRIC PROPERTIES OF THE ANTENNA MODEL

Element	Parameter	Value
dielectric A,B	ε_r	2.17
	thickness	0.25 mm
prepreg	ε_r	2.60
	thickness	0.11 mm
patch	length	1.47 mm
	width	1.45 mm
slots	length	1.57 mm
	width	0.23 mm
	spacing	2.00 mm
reflector	length	2.50 mm
	width	1.80 mm
dipole	length	2.31 mm
	width	0.30 mm

The elements V_m^J of the $\mathbf{V}^J$ vector can be calculated in the spatial domain, whereas the elements Z_{mn}^{PQ} of the $\mathbf{Z}^{PQ}$ matrix have an analytical expression in the spectral domain, e.g.,

$$\begin{aligned} V_m^J &= \int_S \mathbf{J}_m^t(\mathbf{r}) \cdot \mathbf{E}^i(\mathbf{r}) dA, \\ Z_{mn}^{JJ} &= \frac{1}{4\pi^2} \int_{k_\rho} \int_{\alpha} \hat{\mathbf{J}}_m^t(-\mathbf{k}_t, z) \\ &\quad \cdot \left[\underline{\underline{\hat{\mathbf{G}}}}^{EJ}(\mathbf{k}_t, z, z_s) \cdot \hat{\mathbf{J}}_n^e(\mathbf{k}_t, z_s) \right] k_\rho d\alpha dk_\rho, \end{aligned} \tag{3}$$

with $\mathbf{E}^i$ the incident field that is impressed on the structure, $\mathbf{J}^t$ the testing function, $\mathbf{J}^e$ the expansion function, $\underline{\underline{\hat{\mathbf{G}}}}^{EJ}(\mathbf{k}_t, z, z_s)$ the two-dimensional Fourier transform in the horizontal plane of the Green's dyadic $\underline{\underline{\mathbf{G}}}^{EJ}(\mathbf{r}, \mathbf{r}_s)$, which relates the electric field at $\mathbf{r}$ to an electric current $\mathbf{J}$, located at $\mathbf{r}_s$, and $\mathbf{k}_t = k_\rho(\cos(\alpha)\mathbf{u}_x + \sin(\alpha)\mathbf{u}_y)$. The integrals over k_ρ and α are computed numerically by means of contour deformation [23] and Romberg integration [24].

The derived model is used to analyze the radiation efficiency of the antenna in more detail, and to optimize the antenna design. To validate the model, a comparison has been made with commercial full-wave simulation software (Fig. 4 and Table I).

Our model uses 11 rooftop basis functions on the feed, three entire-domain basis functions per slot, three on the reflector, and three on the patch, whereas the commercial software used 510 triangular basis functions. It is observed that the agreement is very good.

IV. Radiation Efficiency

The radiation efficiency and the surface-wave excitation is analyzed in region I (see Fig. 3). In this analysis, the equivalent magnetic current densities, that represent the aperture fields, are considered as the sources in region I. The current densities in both slots are equal owing to the fully symmetric antenna configuration. Consequently, the source power can be written as

$$\begin{aligned} P_s &= -\int_{S_s} \mathbf{M}^t(\mathbf{r}) \cdot \mathbf{H}^*(\mathbf{r}) dA \\ &= -\int_{S_s} \mathbf{M}^t(\mathbf{r}) \cdot \mathbf{H}^{t*}(\mathbf{r}) dA - \int_{S_s} \mathbf{M}^t(\mathbf{r}) \cdot \mathbf{H}^{s*}(\mathbf{r}) dA \\ &= P_s^{\text{slots}} + R_s^{\text{patch}} \end{aligned} \tag{4}$$

with S_s the surface area of the two slots, $\mathbf{M}^t$ the equivalent magnetic current of both the slots, $\mathbf{H}^t$ the magnetic field resulting from the magnetic sources in absence of the patch, and $\mathbf{H}^s$ the magnetic field resulting from the electric current on the patch. The power P_s^{slots} can be interpreted as the power radiated by the two magnetic sources in absence of a patch element and R_s^{patch} can be interpreted as the reaction (or coupling) between the magnetic sources and the scattered magnetic field $\mathbf{H}^s$[25].

The magnetic fields $\mathbf{H}^t$ and $\mathbf{H}^s$ in (4) are found from the spectral Green's dyadics for multilayer dielectric substrates. For example, the reaction between the magnetic source $\mathbf{M}^t$ and the electric current $\mathbf{J}^p$ on the patch is given by

$$\begin{aligned} R_s^{\text{patch}} = \frac{1}{4\pi^2} \int_{k_\rho=0}^{\infty} \int_{\alpha=0}^{2\pi} \hat{\mathbf{M}}^t(-\mathbf{k}_t, z) \\ \cdot \left[\underline{\underline{\hat{\mathbf{G}}}}^{HJ}(\mathbf{k}_t, z, z_s) \cdot \hat{\mathbf{J}}^p(\mathbf{k}_t, z_s) \right]^* k_\rho d\alpha dk_\rho \,. \end{aligned} \tag{5}$$

It is observed that the terms that are needed to determine the source power have already been calculated in order to generate the interaction matrix that is needed for the method-of-moments analysis, owing to the use of Galerkin's method (see Section III).

Part of the source power is dissipated in the dielectric, part is launched into surface waves, and part is radiated. To determine the amount of power that is radiated (P_s^{rad}), the integral over k_ρ in (5) is restricted to $k_\rho \in [0, k_0]$, with k_0 the propagation constant of free space [23]. The power that is confined to the dielectric can now be determined as

$$P_s^{\text{diel}} = P_s - P_s^{\text{rad}} \tag{6}$$

and the radiation efficiency in region I can be defined as

$$\eta^I = \frac{P_s^{\text{rad}}}{P_s}. \tag{7}$$

In Fig. 5, the obtained radiation efficiency is compared to the case where the patch is absent. In this figure the spacing is expressed in terms of the free-space wavelength (λ_0). The calculations have been performed with a single basis function on the slots and a single x-directed basis function on the patch. In Fig. 5, the dimensions of the slots and the patch are given in terms of the wavelength in the dielectric (λ_d). The radiation efficiency that is shown in Fig. 5 has an optimum around $s = \lambda_0/2$ because of the destructive interference of the surface waves that are excited by the slots. It is observed that the presence of the patch significantly increases the radiation efficiency for small slot spacings.

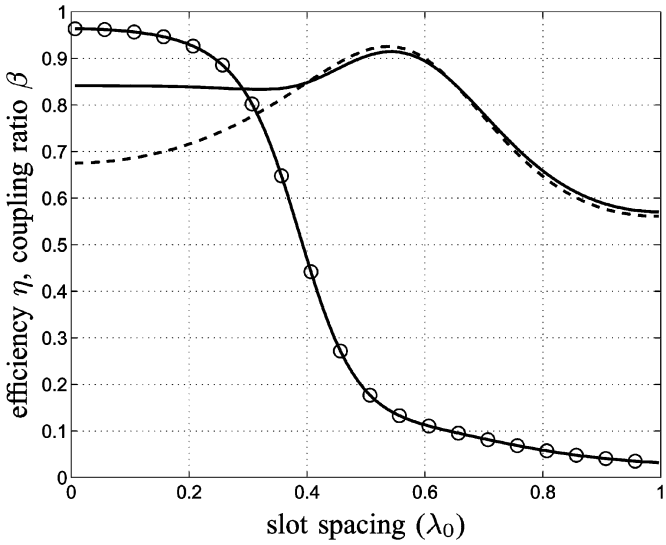

Fig. 5. Efficiency and coupling ratio as a function of slot spacing. Frequency $f = 60$ GHz. Efficiency of slots and patch (solid), efficiency of two slots (dash) and coupling ratio β (circles). Thickness dielectric 0.05 λ_0, $\varepsilon_r = 2.2$, slot length $= \lambda_d/2$, slot width $= \lambda_d/10$, patch length $= \lambda_d/2$, patch width $= \lambda_d/3$.

The spacing between the slots is also important for the operation bandwidth of the antenna. Both the slots and the patch should be used as radiating elements to increase the bandwidth. Hence, the spacing should be chosen such that both elements contribute to the radiated power. To investigate the coupling between the slots and the patch, the coupling ratio β, with reference to (4) and(5), is introduced as

$$\beta = \frac{R_s^{\text{patch}}}{P_s}. \tag{8}$$

The coupling ratio is shown as a function of slot spacing in Fig. 5 as well. From the point of radiation efficiency, a slot spacing around $\lambda_0/2$ is optimal, but, in that case, the patch hardly contributes to the radiated power, and the antenna bandwidth will not benefit from the patch element. A slot spacing in the range from $0.3\lambda_0$ to $0.4\lambda_0$ has been used as a compromise between radiation efficiency and operation bandwidth.

V. Front-to-Back Ratio

The front-to-back ratio κ is defined as

$$\kappa = \frac{P^{\text{rad},I}}{P^{\text{rad},II}} \tag{9}$$

where $P^{\text{rad},i}$ is the power that is radiated into region $i \in \{I, II\}$ (see Appendix I). Note that in this definition the power in the upper and lower hemisphere is compared, instead of the ratio of the Poynting vector in the upward and downward direction. As mentioned in Section II, the front-to-back ratio should be given

consideration in the design of aperture-coupled patch antennas. Especially in this case, where resonating slots are used as radiating elements, the front-to-back ratio can become too low. For a practical design, a front-to-back ratio larger than 10 dB is required. To compensate for the back radiation of the slots, a reflecting metal plane at the back of the antenna can be added [26]. However, this will result in the excitation of a parallel-plate TEM mode between the metal plane and the ground plane, and can seriously degrade the performance. Alternatively, a finite reflector element can be used [16], which is basically a large patch that covers the back of the two radiating slots. The reflector element can be placed at a distance much smaller than $\lambda_d/4$ from the slots, such that the losses in the lower dielectric are limited. In this section, the performances of the infinite PEC plane and the finite reflector element are compared.

The overall efficiency η of the antenna is defined as

$$\eta = \frac{P^{\mathrm{rad},I}}{P^I + P^{II}} \tag{10}$$

with P^i the total power in region i (see Appendix I). Note that in this definition, both regions I and II are considered, whereas, in previous section, the efficiency is considered in region I only. The front-to-back ratio and the overall efficiency are compared for three cases, i.e., no reflector, an infinite reflector (infinite PEC plane), and a finite rectangular reflector. The front-to-back ratio of the infinite reflector is obviously infinite. The front-to-back ratio of the antenna with and without reflector element is shown in the upper graph of Fig. 6. The corresponding antenna dimensions are given in Table I. The efficiency for all three setups is shown in the lower graph of Fig. 6. From this figure, it is clearly seen that the reflector element gives a significant improvement in front-to-back ratio compared to the case where no reflector is present. More importantly, the radiation efficiency of the antenna with the finite reflector element is much larger than the radiation efficiency of the antenna with an infinite metal plane as reflector. The underlying physical principle of the reflector is that it reradiates a field in the backward direction with the same magnitude, with 180° phase difference compared to the fields that are radiated by the slots and the feed structure [16].

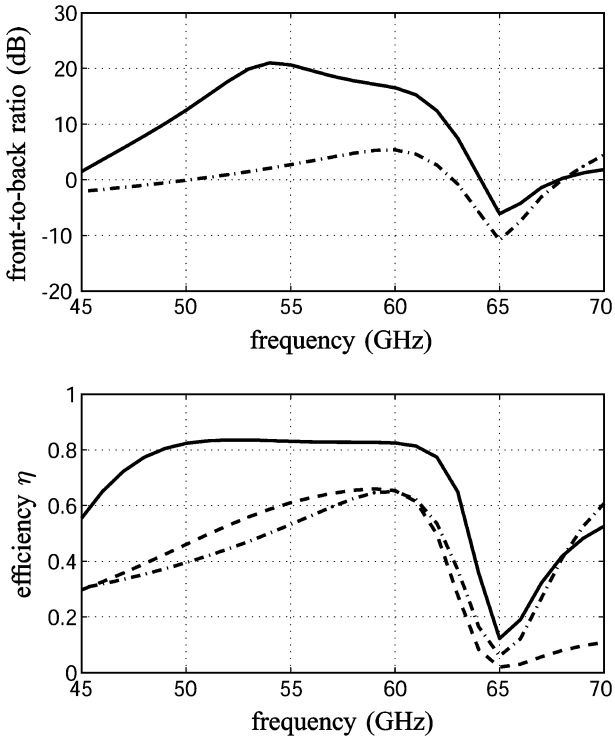

Fig. 6. Front-to-back ratio and radiation efficiency of the antenna. Finite reflector element (solid), infinite reflector (dashed), no reflector (dashed–dotted). Dimensions as in Table I.

VI. Optimization

To further improve the behavior of the antenna, and to assist the design process, we apply an optimization procedure [27]. This optimization procedure employs the derived model (Section III). In general, it is possible to find a good initial estimate of the dimensions of the antenna. For example, the patch length of a patch antenna can be estimated as $l_{\mathrm{patch}} = \lambda_d/2$, with λ_d the wavelength in the dielectric. If it is possible to find an initial guess which lies close to an optimal one, a local optimization strategy can be used to optimize the antenna structure. In this section, some simple design rules for the initial design are given and an optimization approach is proposed.

To implement an efficient and accurate optimization routine, the derivative of the response function to the optimization parameters needs to be determined. This derivative can be determined through a finite-differentiation approximation, but this can introduce serious numerical problems [28]. Therefore, the direct differentiation method [29] is used, which is outlined below, and applied to our MoM model (Section III). Since our MoM model requires a limited number of basis functions, the optimization routine can be efficient as well.

The function $f(\mathbf{p})$ is introduced as the response function of the linear system that depends on the parameter vector $\mathbf{p}$. This function acts as a measure for the performance of the structure. In our case the radiation efficiency and the reflection coefficient of the antenna need to be optimized simultaneously over a certain bandwidth $\omega_0 < \omega < \omega_1$. The proposed response function is given as

$$f(\mathbf{p}) = \frac{1}{\omega_1 - \omega_0} \int_{\omega_0}^{\omega_1} (1 - |\Gamma(\omega, \mathbf{p})|^2)\eta(\omega, \mathbf{p}) d\omega. \tag{11}$$

The reflection coefficient Γ is obtained from

$$\Gamma(\omega, \mathbf{p}) = \frac{Z_{\mathrm{in}}(\omega, \mathbf{p}) - Z_0}{Z_{\mathrm{in}}(\omega, \mathbf{p}) + Z_0} \tag{12}$$

where Z_{in} is the input impedance and Z_0 is the characteristic port impedance of the balanced feed. The radiation efficiency η is found from (10). The sensitivity of the integrand of the response function is written as

$$\nabla_{\mathbf{p}} \Big[(1 - |\Gamma(\omega, \mathbf{p})|^2)\eta(\omega, \mathbf{p}) \Big] = -2\Re\{\Gamma^*(\omega, \mathbf{p}) \nabla_{\mathbf{p}} \Gamma(\omega, \mathbf{p})\} + (1 - |\Gamma(\omega, \mathbf{p})|^2) \nabla_{\mathbf{p}} \eta(\omega, \mathbf{p}). \tag{13}$$

It can be shown (see Appendix II) that $\nabla_{\mathbf{p}}\Gamma$ and $\nabla_{\mathbf{p}}\eta$ can be expressed in terms of $\nabla_{\mathbf{p}}\mathbf{V}$ and $\nabla_{\mathbf{p}}\mathbf{Z}$. It is straightforward to

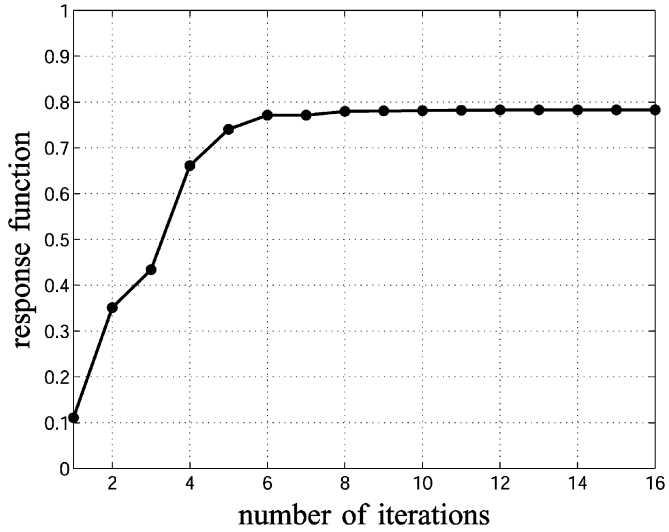

Fig. 7. Convergence of the response function.

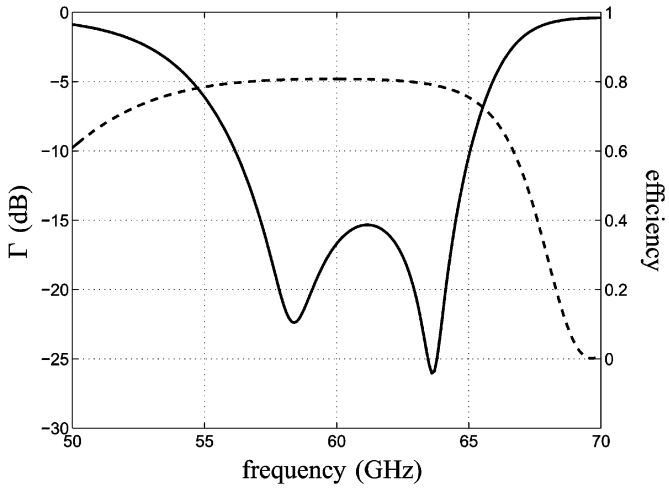

Fig. 8. Reflection coefficient (solid) and radiation efficiency (dashed) of the optimized antenna. Dimensions in Table II.

find an expression for $\nabla_{\mathbf{p}}\mathbf{V}$. For the matrix elements we find, for example,

$$\nabla_{\mathbf{p}} Z_{mn}^{JJ} = \frac{1}{4\pi^2} \int_{k_\rho} \int_{\alpha} \nabla_{\mathbf{p}} \hat{\mathbf{J}}_m^t \cdot \underline{\underline{\hat{\mathbf{G}}}}^{EJ} \cdot \hat{\mathbf{J}}_n^e + \hat{\mathbf{J}}_m^t \cdot \nabla_{\mathbf{p}} \underline{\underline{\hat{\mathbf{G}}}}^{EJ} \cdot \hat{\mathbf{J}}_n^e + \hat{\mathbf{J}}_m^t \cdot \underline{\underline{\hat{\mathbf{G}}}}^{EJ} \cdot \nabla_{\mathbf{p}} \mathbf{J}_n^e k_\rho d\alpha dk_\rho. \quad (14)$$

Once the sensitivity of the response function has been determined, an optimization routine can be used to optimize the response function. The PCB stack that is used for the realization of the antenna is fixed. Therefore, only the geometrical parameters of the antenna have to be optimized. More specifically, the length of the patch, the length of the slots, the spacing of the slots, and the length of the dipole need to be adjusted such that the reflection coefficient as well as the radiation efficiency is optimized in the frequency band from 57 to 64 GHz. Small variations in the dimensions of the reflector element affect the antenna behavior very little because the reflector shows good performance over a wide frequency band. Therefore, the dimensions of the reflector have not been optimized.

As an initial estimate, the patch length has been chosen as $l_{\text{patch}} = \lambda_d^{\text{low}}/2$, with λ_d^{low} the wavelength in the dielectric at the lowest operating frequency (57 GHz). The initial slot length is $l_{\text{slot}} = \lambda_d^{\text{high}}/2$, with λ_d^{high} the wavelength at the highest operating frequency (64 GHz). This ensures that the patch and the slots resonate at slightly different frequencies such that the antenna bandwidth is improved. The initial slot spacing is chosen as $l_{\text{spacing}} = 0.35\ \lambda_0$, which is a compromise between radiation efficiency and coupling between the slots and the patch (see Section IV). The length of the dipole underneath the slots is chosen as $l_{\text{dip}} = l_{\text{spacing}} + w_{\text{slot}}$ such that the dipole has sufficient length to couple with the slots.

In the optimization routine, the integral over ω in (11) is approximated by a finite sum, i.e.,

$$f(\mathbf{p}) = \frac{1}{N} \sum_{n=1}^{N} (1 - |\Gamma(\omega, \mathbf{p})|^2) \eta(\omega_0 + n\Delta_\omega, \mathbf{p}). \quad (15)$$

The response function has been optimized through a conjugate gradient optimization algorithm [30]. The convergence of the response function is shown in Fig. 7. The reflection coefficient and radiation efficiency of the resulting antenna design are shown in Fig. 8. It is observed that this algorithm is able to find an optimum within a few iterations. Moreover, it is shown that this antenna geometry is able to achieve a -10-dB bandwidth of 15% with a radiation efficiency that is larger than 79% throughout the band of operation.

A sensitivity analysis allows for a first-order analysis of the influence of production tolerances on the performance of the antenna. For example the influence of tolerances on the reflection coefficient can be determined as

$$\Gamma(\omega, \mathbf{p} + \boldsymbol{\Delta}) \approx \Gamma(\omega, \mathbf{p}) + \nabla_{\mathbf{p}} \Gamma(\omega, \mathbf{p}) \cdot \boldsymbol{\Delta} \quad (16)$$

where $\boldsymbol{\Delta}$ is a vector that determines the variation of each parameter. Structures in a manufacturing process can be realized with a certain metallization tolerance $\delta_{\max}$. In PCB technology the metallization tolerance is about $\delta_{\max} = \pm 15\ \mu$m. The influence of such variations on the reflection coefficient of the optimized antenna is shown in Fig. 9, where all four parameters used in the optimization have been perturbed by $\delta_{\max}$. It is observed that the reflection coefficient remains well below $-$ 10 dB throughout the band of operation (57–64 GHz). The influence of parameter variations on the radiation efficiency is minimal, i.e., the radiation efficiency varies less than 2% within the band of operation.

Other types of tolerance, like registration tolerance and tolerance on the layer thickness, are possible as well. The sensitivity of antenna performance on these types of tolerances can be analyzed with the presented method as well. However, it is noted that the metallization tolerance is the dominant effect on antenna performance, for our case.

VII. Measurements

The measurement of antennas that operate in the millimeter-wave frequency range is quite challenging. Therefore, a measurement setup is presented that allows for the accurate characterization of the scattering parameters and the radiation pattern of the antenna. The antenna has been realized in a PCB technology. For this realization, the optimized dimensions of

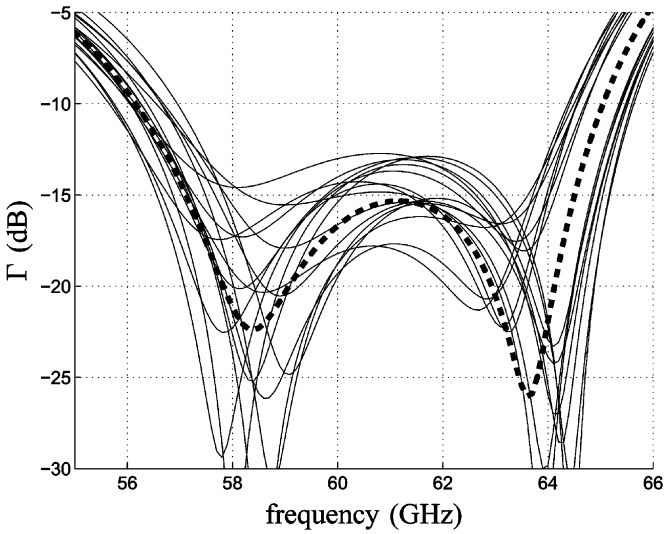

Fig. 9. Tolerance analysis of the reflection coefficient. The patch length, dipole length, slot length, and slot spacing are perturbed with $\delta_{\max} = \pm 15\,\mu$m. Nominal design (dashed), perturbed designs (solid).

TABLE II
DIMENSIONS OF THE OPTIMIZED ANTENNA

Element	Parameter	Value
patch	length	1.38 mm
	width	1.35 mm
slots	length	1.49 mm
	width	0.20 mm
	spacing	1.76 mm
reflector	length	2.50 mm
	width	1.80 mm
dipole	length	2.11 mm
	width	0.25 mm
feed	width	0.20 mm
	spacing	0.15 mm

Table II have been used. The copper thickness is 9 μm. The dielectric that has been chosen for the antenna is Neltec NY9217[1] with a relative dielectric constant of 2.17, specified at 10 GHz. This is among the lowest that are commercially available. Standard layer thicknesses of this board start from 127 μm (5 mils). SpeedBoard C[2] has been used as prepreg. It has a relative dielectric constant of 2.6, specified up to 40 GHz, and it has a minimum layer thickness of 38 μm (1.5 mils). The thickness of dielectric B is chosen as 254 μm (10 mils). This ensures a radiation efficiency in region I larger than 80% for slot spacings well up to $\lambda_0/2$. The thickness of dielectric A is 254 μm as well. The thickness of the prepreg layer equals 112 μm (4.4 mils), which is suited to the design of the feed network since it allows for properly dimensioned 50-Ω transmission lines.

A. Measurement Setup

A measurement setup has been designed to be able to characterize the performance of the antenna. To avoid interconnection problems, RF probes have been used such that a well-defined interconnection between the antenna under test (AUT) and the measurement setup can be realized. RF probes have the advantage that they are reusable, and that they can be calibrated accurately. The use of vias is avoided in the measurement setup to minimize manufacturing uncertainties. Since the realization of vias requires an additional metallization step in the manufacturing process, the copper thickness increases and therefore, the metallization tolerances increase as well. Moreover, additional tolerances on the size and position of the via are introduced. The antenna is realized from two dielectric boards that are stacked with a prepreg layer in between. The feed lines are embedded within the stack. A cavity has been made such that the RF probe can be connected to the feed lines. The cavity has been realized by creating a hole in the upper dielectric board and in the prepreg board before the boards are stacked together.

[1]Nelco N9000 PTFE Laminates, Park Electrochemical Corp.

[2]Gore Speedboard C Prepreg Data Sheet, W. L. Gore & Associates.

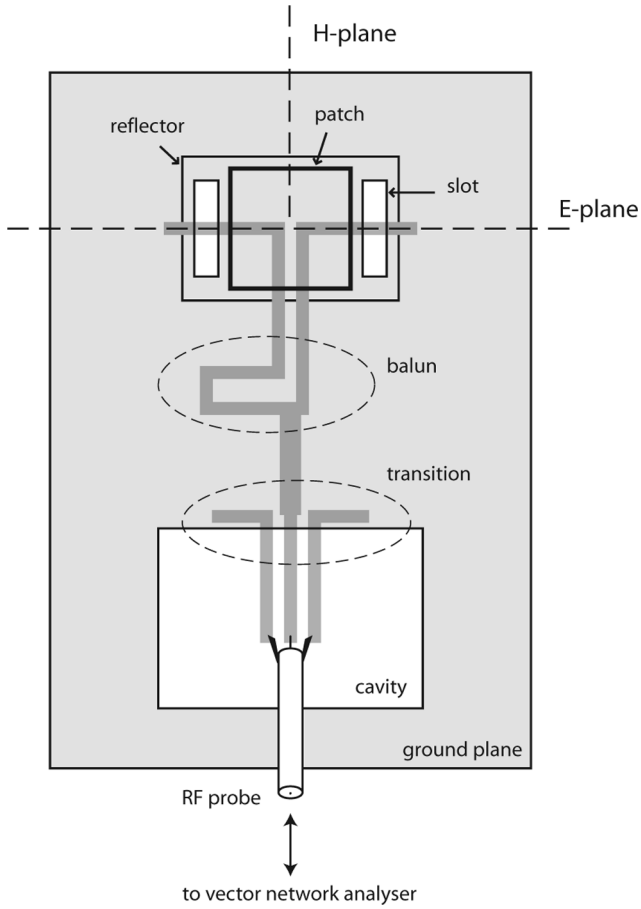

Fig. 10. Schematic layout of AUT and measurement setup.

A schematic layout of the AUT and the measurement setup is shown in Fig. 10. Since the antenna has a balanced feed, a balun is required that transforms the balanced coupled microstrip line to an unbalanced microstrip line. The RF probe has to land on a coplanar waveguide (CPW) transmission line. To connect to the balun, a transition from CPW to microstrip (MS) is needed. This transition is realized without the use of vias. Instead, two quarter-wavelength stubs are attached to both ground lines of the CPW to provide a virtual ground at the end of the CPW line, following an idea by Raskin *et al.* [31]. A photograph of the antenna with RF probe is shown in Fig. 11. The size of the dielectric boards and the ground plane is 20×35 mm.

The balun design is straightforward. The microstrip line connects to two lines that have a length difference which corresponds to 180° of phase difference at 60 GHz. These two lines are immediately connected to the coplanar microstrip (CPS) transmission line that is used to feed the antenna. A challenge in the measurement of the reflection coefficient of the antenna is

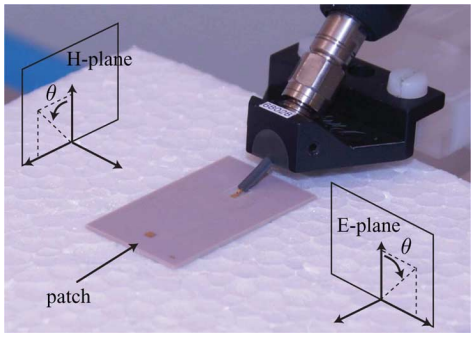

Fig. 11. Photograph of antenna and RF probe. The E-plane, H-plane, and elevation angle θ are indicated in the picture.

to de-embed the CPW to MS transition from the measurements. For this purpose, additional structures have been realized on the antenna board. Three different types of transitions in a back-to-back configuration have been realized, i.e., an open, a through, and a line configuration. In this way, all the S-parameters of the transition can be characterized following a TRL calibration procedure [32]. Although the measured performance of the CPW-MS transition is not exactly the simulated performance (see [33]), it has been observed that measurements over a batch of realized cavities are consistent, and therefore it is possible to use this calibration technique.

Since it is already challenging to accurately de-embed the cavity transition from the measurements, we present measured results that include the balun. The measured and simulated reflection coefficients of the combined antenna and balun after de-embedding are shown in Fig. 12. The simulation has been performed with Ansoft Designer, since the balun is not included in the model that is derived in Section III. The metal thickness of the feed lines has been included in the simulation to obtain more accurate results. Good agreement between measurement and simulation is observed within the operation bandwidth. The resonances of the slots and the patch can be recognized in the measured and simulated Γ curves. It is observed that the balun introduces some additional mismatch since the simulated reflection coefficient of the antenna without balun remains well below -10 dB (see Fig. 8). It is shown that the simulations and the measurements are in good agreement. Therefore, it is plausible that the performance of the antenna alone is also in good agreement with simulations.

B. Radiation Pattern

To determine the radiation pattern of the antenna, a far-field measurement setup has been built [33]. This setup has been tailored to the measurement of the radiation pattern of millimeter-wave antennas and antenna arrays. The radiation pattern of the antenna has been measured in the frequency range from 40 to 67 GHz. The measurements have been conducted in a normal lab environment. To reduce the influence of the environment, time-gating has been applied [33]. The resulting radiation pattern in the E-plane (see Fig. 11) is shown in Fig. 13, and is compared with two simulations, i.e., a planar simulation (Ansoft Designer) and a 3-dimensional (3-D) simulation (CST microwave studio). In the 3-D simulations, the influence of the finite size of the dielectric layers has been included.

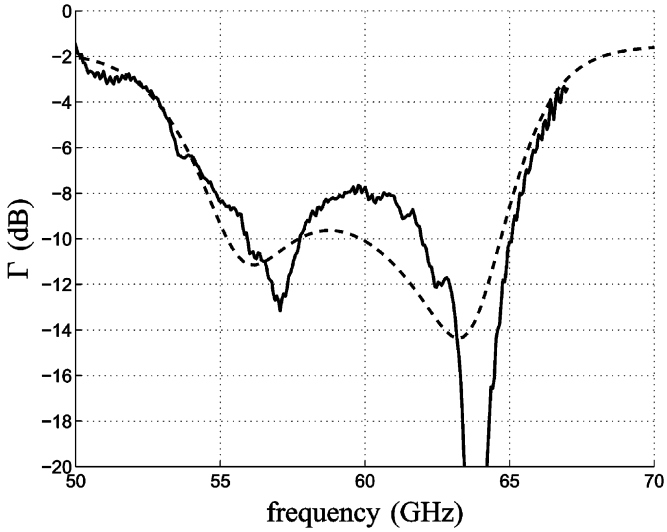

Fig. 12. Measured (solid) and simulated (dashed) reflection coefficient of the antenna in combination with the balun.

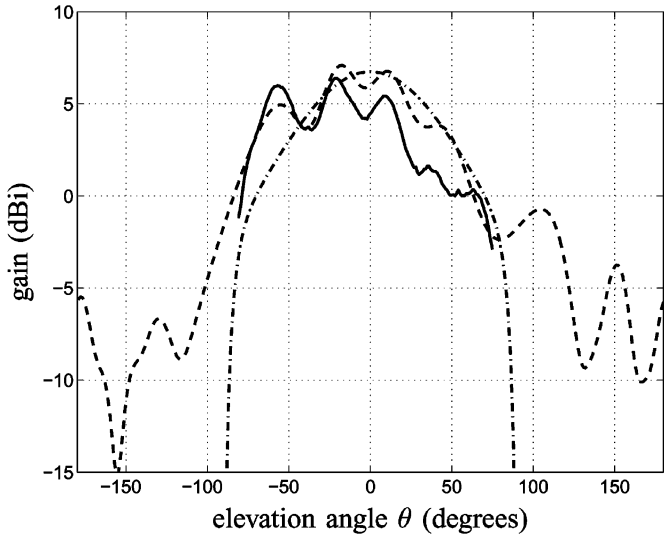

Fig. 13. Radiation pattern of the combined antenna and balun. E-plane, $f = 60$ GHz. Measurement (solid), 3-D simulation (dashed), planar simulation (dashed–dotted).

Two important things can be observed from this figure. First, the difference between the simulated patterns clearly shows the effect of the finite size of the dielectric on the radiation pattern. Due to the scattered surface waves at the edges of the dielectric, a ripple is superimposed on the radiation pattern resulting from the planar simulation (Section III). Second, it is shown that the agreement of the measurement and the 3-D simulation is rather good. The radiation pattern shows some asymmetry, which is introduced by the balun. Because of the balun, the slots are not excited exactly in phase. Therefore, the main lobe of the antenna is tilted towards $\theta \approx -20^\circ$ in the E-plane. The ripple that is caused by the radiation from the edges of the dielectric results in the dips in the radiation pattern at $\theta = -40^\circ$ and 0°. Fig. 13 shows that this effect can be measured as well.

The difference in simulated and measured gain is approximately 2 dB. This loss is mainly caused by the feed line that

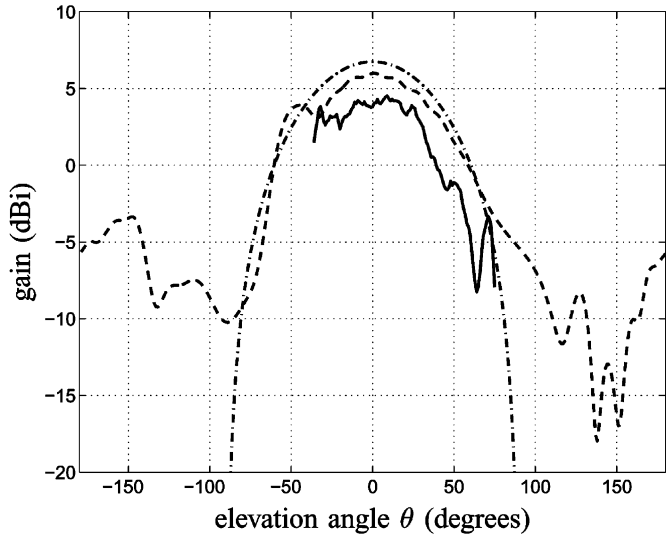

Fig. 14. Radiation pattern of the combined antenna and balun. H-plane, $f = 60$ GHz. Measurement (solid), 3-D simulation (dashed), planar simulation (dashed–dotted).

connects the RF probe and the antenna. The total length from probe tip to antenna is 1.5 cm, which results in a feed-line loss of $2/1.5 = 1.3$ dB/cm. Although, this is a rough estimate since the feed line includes the CPW to MS transition and the balun, the value is comparable to simulation results that predict a loss of about 1.2 dB/cm for a microstrip transmission line with a copper thickness of 9 μm. The back radiation increases due to the presence of the feed network. Especially the balun introduces some additional back radiation. To verify this, the finite antenna with balanced feed is analyzed in a 3-D simulation. In this case, the back radiation remains well below -10 dBi.

The H-plane radiation pattern is shown in Fig. 14. The measurement in this plane could not be performed all the way up to $\theta = -90^\circ$ since the RF probe blocks the radiation in that region (see Fig. 11). However, good agreement is observed in the measurement region.

VIII. Antenna Array

In a millimeter-wave transceiver, an antenna array consisting of balanced-fed aperture-coupled patch antenna elements will be connected to a transceiver chip, which has balanced interconnections to each antenna element. As long as the active electronics are located close to the antenna, the feed-line loss is limited and the antenna efficiency will be close to the estimated efficiency of 80%. To validate the performance of the antenna element in an array configuration, a six-element circular array with a fixed feed network has been designed (Fig. 15). Here, the feed network for the array is designed with microstrip transmission lines and baluns have been used to implement the conversion from microstrip to coupled microstrip at each antenna element. This approach is similar to the measurement setup that has been used for the single element antenna. For the power division, Bagley power dividers [34] and reactive T-junctions have been used. The radiation pattern of the antenna array is shown in Fig. 16. The losses in the feed network are not included in the gain measurement to be able to compare the antenna gain with the simulated gain. The loss in the feed network from probe tip

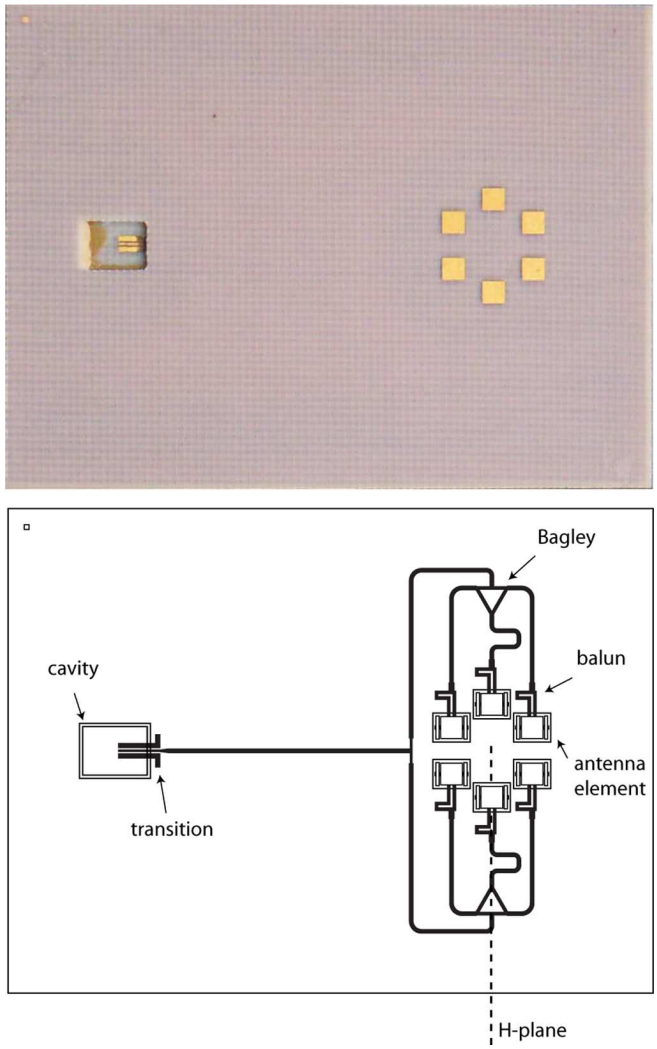

Fig. 15. Layout of the six-element circular array with fixed feed network. Top: Photograph of realized antenna array, bottom: antenna array layout. The size of the dielectric boards and the ground plane is 30 × 40 mm.

to antenna element has been estimated as 4.5 cm × 1.3 dB/cm, which is 5.9 dB. The estimated feed-line loss of 1.3 dB/cm is obtained from the single-element antenna measurement. It is observed that the measured pattern is in good agreement with the simulated pattern. The measured gain is 11.8 dBi, whereas 12.6 dBi is simulated.

IX. Conclusion

A balanced-fed aperture-coupled patch antenna element has been presented that is tailored for broadband millimeter-wave communication. It can be realized in low-cost PCB technology, has a high radiation efficiency, and can be integrated with balanced RF electronics. It has been shown that the antenna can be modeled and optimized with a method-of-moments approach which employs a limited number of entire-domain basis functions. The influence of slot-spacing on radiation efficiency has been analyzed, and the performance of the reflector element has been investigated. To simplify the design of the antenna, design rules have been given and the antenna is optimized for operation bandwidth as well as radiation efficiency. The antenna element has been realized, and the measured performance is close to the expected one. The measured gain including feed-line losses is

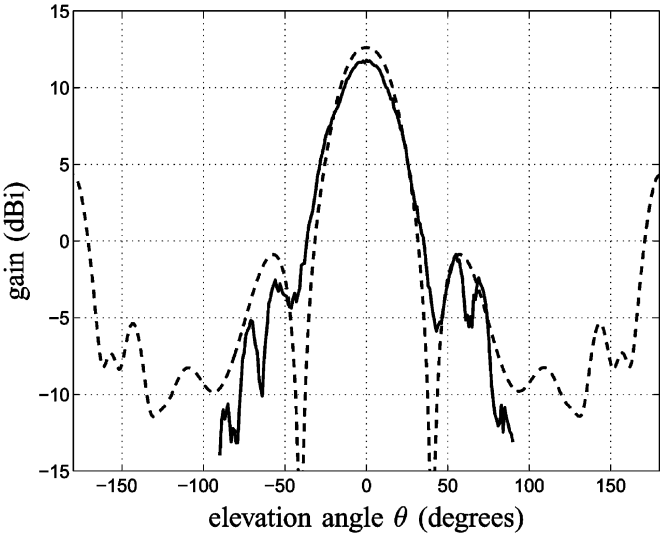

Fig. 16. Radiation pattern of the circular six-element array. H-plane, f = 60.0 GHz. Measurement (solid), 3-D simulation (dashed).

about 4 dBi. A circular six-element antenna array has been realized and characterized as well. The performance of this array is also in agreement with simulations, and has a measured gain of 12 dBi.

APPENDIX I

The total power in region i can be calculated as

$$P^i = I^{i\,H}\mathbf{Z}^i I^i \tag{17}$$

where I^i represents the current vector with electric and/or magnetic currents that are present in region i, and $\mathbf{Z}^i$ represents the interaction matrix that is related to these currents. The superscript H denotes the Hermitian transpose. The radiated power can be calculated as

$$P^{\mathrm{rad},i} = I^{i\,H}\mathbf{Z}^{k_0,i} I^i. \tag{18}$$

The matrix $\mathbf{Z}^{k_0,i}$ represents the matrix $\mathbf{Z}^i$ of (17) with the integral over k_ρ of the matrix terms restricted to $k_\rho \in [0, k_0]$, as explained in Section IV.

APPENDIX II

It is shown that the derivative of the reflection coefficient $\Gamma(\omega, \mathbf{p})$ and the radiation efficiency $\eta(\omega, \mathbf{p})$ with respect to the parameter vector $\mathbf{p}$ can be expressed in terms of $\nabla_{\mathbf{p}}\mathbf{V}$ and $\nabla_{\mathbf{p}}\mathbf{Z}$. The derivative of the reflection coefficient can be determined as

$$\begin{aligned}\nabla_{\mathbf{p}}\Gamma(\omega,\mathbf{p}) &= \nabla_{\mathbf{p}}\frac{Z_{\mathrm{in}}(\omega,\mathbf{p})-Z_0}{Z_{\mathrm{in}}(\omega,\mathbf{p})+Z_0}\\ &= \frac{\nabla_{\mathbf{p}}Z_{\mathrm{in}}(\omega,\mathbf{p})}{Z_{\mathrm{in}}(\omega,\mathbf{p})+Z_0}\\ &\quad - \frac{Z_{\mathrm{in}}(\omega,\mathbf{p})-Z_0}{(Z_{\mathrm{in}}(\omega,\mathbf{p})+Z_0)^2}\nabla_{\mathbf{p}}Z_{\mathrm{in}}(\omega,\mathbf{p}).\end{aligned} \tag{19}$$

From this point on, the dependencies of $\mathbf{V}(\omega,\mathbf{p}), \mathbf{I}(\omega,\mathbf{p})$ and $\mathbf{Z}(\omega,\mathbf{p})$ are omitted. The derivative of the input impedance is written as

$$\nabla_{\mathbf{p}}Z_{\mathrm{in}}(\omega,\mathbf{p}) = \nabla_{\mathbf{p}}\frac{\mathbf{V}_k}{\mathbf{I}_k} = \frac{\nabla_{\mathbf{p}}\mathbf{V}_k}{\mathbf{I}_k} - \frac{\mathbf{V}_k}{\mathbf{I}_k^2}\nabla_{\mathbf{p}}\mathbf{I}_k \tag{20}$$

where $\mathbf{V}_k, \mathbf{I}_k$ denotes the kth element of the vectors $\mathbf{V}$ and $\mathbf{I}$, which represent the voltage and current at the port. The derivative of the current can be expressed as

$$\nabla_{\mathbf{p}}\mathbf{I} = \nabla_{\mathbf{p}}[\mathbf{Z}^{-1}\mathbf{V}] = \mathbf{Z}^{-1}\Big(\nabla_{\mathbf{p}}\mathbf{V} - [\nabla_{\mathbf{p}}\mathbf{Z}]\mathbf{I}\Big). \tag{21}$$

The derivative of the radiation efficiency is found from

$$\begin{aligned}&\nabla_{\mathbf{p}}\eta(\omega,\mathbf{p})\\ &\quad= \nabla_{\mathbf{p}}\frac{P^{\mathrm{rad},I}(\omega,\mathbf{p})}{P^I(\omega,\mathbf{p})+P^{II}(\omega,\mathbf{p})}\\ &\quad= \frac{\nabla_{\mathbf{p}}P^{\mathrm{rad},I}(\omega,\mathbf{p})}{P^I(\omega,\mathbf{p})+P^{II}(\omega,\mathbf{p})}\\ &\quad\quad- \frac{P^{\mathrm{rad},I}(\omega,\mathbf{p})\left[\nabla_{\mathbf{p}}(P^I(\omega,\mathbf{p})+P^{II}(\omega,\mathbf{p}))\right]}{(P^I(\omega,\mathbf{p})+P^{II}(\omega,\mathbf{p}))^2}\end{aligned} \tag{22}$$

where the derivative of the radiated power in Region I is

$$\begin{aligned}&\nabla_{\mathbf{p}}P^{\mathrm{rad},I}(\omega,\mathbf{p})\\ &\quad= \nabla_{\mathbf{p}}\frac{1}{2}\Re\left\{\mathbf{I}^H\mathbf{Z}^{k_0}\mathbf{I}\right\}\\ &\quad= \frac{1}{2}\Re\Big\{\left[\nabla_{\mathbf{p}}\mathbf{I}^H\right]\mathbf{Z}^{k_0}\mathbf{I} + \mathbf{I}^H\left[\nabla_{\mathbf{p}}\mathbf{Z}^{k_0}\right]\mathbf{I} + \mathbf{I}^H\mathbf{Z}^{k_0}[\nabla_{\mathbf{p}}\mathbf{I}]\Big\}.\end{aligned} \tag{23}$$

The matrix $\mathbf{Z}^{k_0}$ represents the matrix $\mathbf{Z}$ of (2) with the integral over k_ρ of the matrix terms restricted to $k_\rho \in [0, k_0]$, as explained in Section IV. Finally, the derivative of the total power is obtained as

$$\begin{aligned}&\nabla_{\mathbf{p}}(P^I(\omega,\mathbf{p})+P^{II}(\omega,\mathbf{p}))\\ &\quad= \nabla_{\mathbf{p}}\frac{1}{2}\Re\{\mathbf{I}^H\mathbf{Z}\mathbf{I}\}\\ &\quad= \frac{1}{2}\Re\Big\{\left[\nabla_{\mathbf{p}}\mathbf{I}^H\right]\mathbf{Z}\mathbf{I} + \mathbf{I}^H[\nabla_{\mathbf{p}}\mathbf{Z}]\mathbf{I} + \mathbf{I}^H\mathbf{Z}[\nabla_{\mathbf{p}}\mathbf{I}]\Big\}.\end{aligned} \tag{24}$$

ACKNOWLEDGMENT

The authors would like to thank M. van der Graaf and R. van Dijk for their help in the realization and measurement of the antenna characteristics at the laboratory of TNO Defence, Security and Safety in The Hague, The Netherlands. The authors also thank R. Mahmoudi for his help with the measurement at the Mixed-Signal Microelectronics group at the Eindhoven University of Technology.

REFERENCES

[1] "Code of Federal Regulation, Title 47 Telecommunication," U.S. Federal Communication Commission, Tech. Rep. part 15.255, 2004.

[2] C. Doan, S. Emami, A. Niknejad, and R. Brodersen, "Design of CMOS for 60 GHz applications," in *Solid-State Circuits Conf. Dig. Tech. Papers*, 2004.
[3] P. Smulders, "Exploiting the 60 GHz band for local wireless multimedia access: Prospects and future directions," *IEEE Commun. Mag.*, vol. 40, pp. 140–147, Jan. 2002.
[4] Y. Zhang, M. Sun, K. Chua, L. Wai, D. Liu, and B. Gaucher, "Antenna-in-package in LTCC for 60-GHz radio," in *Proc. Int. Workshop Antenna Technology*, Mar. 2007.
[5] N. Alexopoulos, P. Katehi, and D. Rutledge, "Substrate optimization for integrated circuit antennas," *IEEE Trans. Microw. Theory Tech.*, vol. 83, pp. 550–557, Jul. 1983.
[6] D. Jackson, J. Williams, A. Bhattacharyya, R. S. S. Buchheit, and S. Long, "Microstrip patch designs that do not excite surface waves," *IEEE Trans. Antennas Propag.*, vol. 41, pp. 1026–1037, Aug. 1993.
[7] G. Gauthier, A. Courtay, and G. Rebeiz, "Microstrip antennas on synthesized low dielectric-constant substrates," *IEEE Trans. Antennas Propag.*, vol. 45, pp. 1310–1314, Aug. 1997.
[8] A. Weily, L. Horvath, K. Esselle, B. Sanders, and T. Bird, "A planar resonator antenna based on a woodpile EBG material," *IEEE Trans. Antennas Propag.*, vol. 53, pp. 216–223, Jan. 2005.
[9] F. Yang and Y. Rahmat-Samii, "Reflection phase characterizations of the EBG ground plane for low profile wire antenna applications," *IEEE Trans. Antennas Propag.*, vol. 51, pp. 2691–2703, Oct. 2003.
[10] N. Llombart, A. Neto, G. Gerini, and P. de Maagt, "Planar circularly symmetric EBG structures for reducing surface waves in printed antennas," *IEEE Trans. Antennas Propag.*, vol. 53, pp. 3210–3218, Oct. 2005.
[11] T. Zwick, D. Liu, and B. Gaucher, "Broadband planar superstrate antenna for integrated millimeterwave transceivers," *IEEE Trans. Antennas Propag.*, vol. 54, pp. 2790–2796, Oct. 2006.
[12] J. Akkermans and M. Herben, "Planar beam-forming array for broadband communication in the 60 GHz band," in *Proc. Eur. Conf. Antennas Propagation*, Edinburgh, U.K., Nov. 2007, pp. 1–6.
[13] J. Akkermans, M. van Beurden, and M. Herben, "Design of a millimeter-wave balanced-fed aperture-coupled patch antenna," presented at the Eur. Conf. Antennas Propagation, Nice, France, Nov. 2006.
[14] T. Brauner, R. Vogt, and W. Bachtold, "A differential active patch antenna element for array applications," *IEEE Microw. Wireless Compon. Lett.*, vol. 13, pp. 161–163, Apr. 2003.
[15] D. Pozar, "A microstrip antenna aperture coupled to a microstrip line," *Electron. Lett.*, vol. 21, pp. 49–50, Jan. 1985.
[16] S. Targonski and R. Waterhouse, "Reflector elements for aperture and aperture coupled microstrip antennas," in *Proc. Antennas Propagation Soc. Int. Symp.*, Jul. 1997, vol. 3, pp. 1840–1843.
[17] G. V. Eleftheriades and M. Qiu, "Efficiency and gain of slot antennas and arrays on thick dielectric substrates for millimeter-wave applications: A unified approach," *IEEE Trans. Antennas Propag.*, vol. 50, pp. 1088–1098, Aug. 2002.
[18] J. Huang, "The finite ground plane effect on the microstrip antenna radiation patterns," *IEEE Trans. Antennas Propag.*, vol. 31, pp. 649–653, Jul. 1983.
[19] E. Rothwell and M. Cloud, *Electromagnetics*. Boca Raton, FL: CRC Press, 2001.
[20] P. L. Sullivan and D. H. Schaubert, "Analysis of an aperture coupled microstrip antenna," *IEEE Trans. Antennas Propag.*, vol. 34, pp. 977–984, Aug. 1986.
[21] N. K. Das and D. M. Pozar, "A generalized spectral-domain Green's function for multilayer dielectric substrates with application to multilayer transmission lines," *IEEE Trans. Microw. Theory Techniques*, vol. 35, pp. 326–335, Mar. 1987.
[22] K. A. Michalski and J. R. Mosig, "Multilayered media Green's functions in integral equation formulations," *IEEE Trans. Antennas Propag.*, vol. 45, pp. 508–519, Mar. 1997.
[23] J. Wait, *Electromagnetic Waves in Stratified Media*, reissued ed. New York: IEEE, 1996.
[24] W. Press, S. Teukolsky, and W. Vetterling, *Numerical Recipes in C++*, 2nd ed. Cambridge, U.K.: Cambridge Univ. Press, 2002.
[25] V. Rumsey, "Reaction concept in electromagnetic theory," *Phys. Rev.*, vol. 94, pp. 1483–1491, Jun. 1954.
[26] M. Qiu, M. Simcoe, and G. Eleftheriades, "Radiation efficiency of printed slot antennas backed by a ground reflector," in *Proc. Antennas Propagation Soc. Int. Symp.*, Jul. 2000, vol. 3, pp. 1612–1615.
[27] J. Akkermans and M. Herben, "Sensitivity analysis and optimisation of electromagnetic structures," presented at the Electromagnetics Theory Symp., Ottawa, Canada, Jul. 2007.
[28] G. Evans, *Practical Numerical Analysis*. New York: Wiley, 1995.
[29] S. Amari, P. Harscher, R. Vahldieck, and J. Bornemann, "Novel analytic gradient evaluation techniques for optimization of microwave structures," in *IEEE MTT-S Int. Microwave Symp. Dig.*, Jun. 1999, vol. 1, pp. 31–34.
[30] Numerical Algorithms Group Library [Online]. Available: http://www.nag.co.uk
[31] J.-P. Raskin, G. Gauthier, L. P. Katehi, and G. M. Rebeiz, "W-band single-layer vertical transitions," *IEEE Trans. Microw. Theory Tech.*, vol. 48, pp. 161–164, Jan. 2000.
[32] D. Pozar, *Microwave Engineering*, 3rd ed. New York: Wiley, 2005.
[33] J. Akkermans, R. van Dijk, and M. Herben, "Millimeter-wave antenna measurement," in *Eur. Microwave Conf.*, München, Germany, Oct. 2007, pp. 83–86.
[34] A. W. Rudge, K. Milne, A. Olver, and P. Knight, *The Handbook of Antenna Design*. London, U.K.: Institution of Engineering and Technology, 1983.

Johannes A. G. Akkermans received the M.Sc. degree in electrical engineering and the Ph.D. degree both from the Eindhoven University of Technology, Eindhoven, The Netherlands, in 2004 and 2009, respectively.

His research focuses on the design of antennas for broadband communication at millimeter-wave frequencies. His other research interests include wireless power transfer, electromagnetic modeling, and antenna measurement.

Matti H. A. J. Herben (S'79–M'83–SM'88) was born in Klundert, The Netherlands, in 1953. He received the M.Sc. degree (*cum laude*) in electrical engineering and the Ph.D. degree in technical sciences from the Eindhoven University of Technology (TU/e), The Netherlands, in 1978 and 1984, respectively.

Since 1978, he has been with the Department of Electrical Engineering, TU/e, where he is currently an Associate Professor. His research interests and publications are in the areas of antennas, radio wave propagation, channel modeling for wireless communications, and atmospheric remote sensing.

Dr. Herben was Associate Editor of *Radio Science* from 1993 to 1996 and since 2007 has been Associate Editor of the IEEE TRANSACTIONS ON ANTENNAS AND PROPAGATION. He is a member of the Royal Institute of Engineers (KIvI), the Dutch Electronics and Radio Society (NERG), the Dutch URSI-Committee, the Executive Committee of the IEEE Benelux Chapter on Communications and Vehicular Technology, and the Management Committee of COST Action 2100—"Pervasive Mobile Ambient Wireless Communications."

Martijn C. van Beurden received the M.Sc. and Ph.D. degree in electrical engineering (both *cum laude*) from the Eindhoven University of Technology, The Netherlands, in 1997 and 2003, respectively.

Since 2000, he has been an Assistant Professor in the Department of Electrical Engineering of the Eindhoven University of Technology. His current research interest involves efficient numerical modeling techniques in the context of stochastic and design problems in electromagnetics.

Dr. van Beurden won the second prize of the IEEE Region 8 student paper contest and the C.I.V.I.-prize 1998 for electrical engineering, both for his M.Sc. thesis on the analysis of phased arrays of printed antennas. In 2004, he received the ASML prize for the best Ph.D. Thesis on Applied Research in 2003 of the Eindhoven University of Technology.